Thermal and Thermomechanical Phenomena in Picosecond Laser Copper Interaction

Xinwei Wang
e-mail: xwang3@unl.edu
Department of Mechanical Engineering,
N104 Walter Scott Engineering Center,
The University of Nebraska at Lincoln,
Lincoln, Nebraska 68588-0656

Thermal and thermomechanical phenomena in laser metal interaction are of great importance in terms of understanding the underlying mechanisms in laser materials processing, optimizing the efficiency of laser micro-machining, and minimizing laser induced damage. In this work, Molecular Dynamics (MD) simulation is carried out to investigate picosecond laser copper interaction. A method has been developed to account for the laser beam absorption in, and the thermal transport sustained by, free electrons. Superheating is observed, and an evident temperature drop is revealed at the solid-liquid interface, which moves at a speed of 4400 m/s. However, the later phase change from solid to liquid happens in the target simultaneously and no visible movement of solid-liquid interface is observed. The results show that the laser induced stress wave consists of a strong compressive stress and a weak tensile stress. After reflection at the back side of the MD domain, the strong compressive stress becomes a strong tensile stress, which results in a visible drop of the number density of atoms. In the presence of this strong tensile stress, voids have formed in the region near the back side of the MD domain, indicating that the strong tensile stress in laser materials interaction plays an important role in terms of inducing structural damage. [DOI: 10.1115/1.1725092]

Keywords: *Heat Transfer, Laser, Stress, Thermal*

I Introduction

Thermal and thermomechanical phenomena in laser materials interaction have attracted much attention due to the rapid development of lasers and their applications in materials processing. Laser metal interaction differs from laser dielectric interaction in terms of laser absorption and thermal transport mechanisms. In dielectrics, the laser energy is directly absorbed by molecules and the laser induced thermal transport is sustained by the vibration movement of molecules. On the other hand, in metals the laser energy is absorbed by free electrons, thereby resulting in a temperature gradient in electrons and a temperature difference between electrons and the lattice. The lattice is subsequently heating up through the energy exchange between electrons and the lattice [1].

Attributed to ultrafast laser metal heating and the resulting intense structural change, Molecular Dynamics (MD) simulations have been employed to investigate the pertaining thermal and thermomechanical phenomena at atomic levels. By incorporating the energy transfer from electrons to lattice, Häkkinen and Landman [2] have investigated the superheating, melting, and annealing of copper surfaces under picosecond (ps: 10^{-12} second) laser irradiation. Applying the Morse potential [3] to two-dimensional MD simulation, Horiuchi et al. [4] investigated ps laser induced ablation in Fe and compared the results with experiments quantitatively. However, it needs to be pointed out that MD simulations using the Morse potential do not take account of the thermal transport sustained by the movement of free electrons, which accounts for the major thermal transport in metals. In order to account for the thermal transport by free electrons, Ohmura et al. [5] modified the MD simulation using the Morse potential by implementing a forced thermal conduction among atoms. Using this modified MD simulation, they studied the temperature field and laser induced ablation in ps laser Al interaction.

It is worth noting that during laser metal interaction, the laser energy is absorbed by free electrons, and then free electrons transfer the energy to the lattice. This two-step heating has significant effects on laser induced thermal and thermomechanical phenomena [6–8]. In addition, due to the high thermal conductance nature of metals, the limited size of targets in MD simulation imposes much constraint on thermal transport, thereby inducing unrealistic phenomena in laser induced material ablation.

In this work, MD simulation is modified a great deal to study thermal and thermomechanical phenomena in ps laser copper interaction. The laser beam absorption in, and the thermal transport sustained by free electrons, and the energy exchange between electrons and the lattice are taken into account to give a detailed picture of laser copper interaction. Special treatment of boundary conditions at the back side of the MD domain is introduced to simulate a semi-infinite material irradiated by a ps laser pulse. Emphasis is placed on stress wave reflection from the back side of the MD domain and its strong influence on the structural damage. Methodologies of the MD simulation are described in Sec. II and simulation results are presented in Sec. III.

II Simulation Methods

The problem to be addressed is associated with a copper crystal at an initial temperature of 300 K illuminated with a ps laser pulse. The basic procedure is to solve the Newtonian equation for each atom interacting with its neighbors,

$$m_i \frac{d^2 r_i}{dt^2} = \sum_{j \neq i} F_{ij} \tag{1}$$

where m_i and r_i are the mass and position of atom *i*, respectively. F_{ij} is the interaction force between atoms *i* and *j*, which is calculated from the Morse potential as $F_{ij} = -\partial \phi_{ij} / \partial r_{ij}$ with $r_{ij} = r_i - r_j$. The Morse potential ϕ_{ij} takes the form of [3]

$$\phi_{ij} = D(e^{-2\sigma(r_{ij}-r_0)} - 2e^{\alpha(r_{ij}-r_0)}) \tag{2}$$

where D is the dissociation energy, r_0 is the equilibrium distance of atoms, and α is a constant of the dimension of reciprocal distance.

Contributed by the Heat Transfer Division for publication in the JOURNAL OF HEAT TRANSFER. Manuscript received by the Heat Transfer Division March 31, 2003; revision received January 21, 2004. Associate Editor: C. P. Grigoropoulos.

Table 1 Values of the parameters used in the MD simulation [3,10,12–15]

Parameters	Values
Atomic mass, m (kg)	1.055×10^{-25}
Dissociation energy, D (eV)	0.3429
Constant, α (m^{-1})	1.3588×10^{10}
Lattice constant of copper, a (nm)	0.361
Equilibrium distance, r_0 (nm)	0.2866
Time step, δt (fs)	5
Electron-lattice coupling, G ($\mathrm{W/m^3\cdot K}$)	4.8×10^{16}
Volumetric specific heat of free electrons, C_e ($\mathrm{J/m^3\cdot K}$)	2.1×10^{4}
Thermal conductivity of free electrons, k_e ($\mathrm{W/m\cdot K}$)	386
Volumetric specific heat of lattice, C_l ($\mathrm{J/m^3\cdot K}$)	3.439×10^{6}
Laser beam absorption depth, τ (nm)	12.60
t_0 (ps)	10
t_1 (ps)	3
Laser fluence, E ($\mathrm{J/m^2}$)	2000

Values of these parameters used in the calculation are listed in Table 1. In the calculation, the half-step leap-frog scheme, a modification to the velocity Verlet algorithm [9], is employed to solve the movement of atoms with a time step of 5 fs (fs: 10^{-15} second). When the distance between atoms exceeds a certain value r_c, namely the cutoff distance, the interaction between them is negligible, and no force computation is necessary. The cutoff distance is chosen to make sure that the neglected interaction force is much smaller than the typical force between atoms. In this work, it is found that a cutoff distance of 0.684 nm is appropriate in terms of the uncertainty and computation time requirement. At this distance, the potential of an atomic-pair is less than 1% of the well depth of the Morse potential. The force between two atoms of a distance of 0.684 nm is less than 0.2% of the force (the typical force) between two nearest neighboring atoms in equilibrium positions.

Pulsed laser heating in the target is achieved in two steps. First, the laser beam is absorbed by free electrons following the equation [1,6]

$$C_e\frac{\partial T_e}{\partial t}=k_e\frac{\partial^2 T_e}{\partial z^2}-G(T_e-T_l)+I\cdot\tau^{-1}\cdot e^{-z/\tau} \tag{3}$$

where C_e, T_e, and k_e are the volumetric specific heat, temperature, and thermal conductivity of free electrons, respectively. T_l stands for the lattice temperature, G is the electron-lattice coupling constant, and z is the direction normal to the target surface. Equation (3) describes the evolution of the temperature of free electrons under thermal diffusion, laser heating, and electron-lattice coupling. The laser beam is assumed to be absorbed exponentially with a characteristic absorption depth τ. The wavelength of the laser beam is presumed to be 0.8 μm, which is the wavelength of the Ti:sapphire ps laser. At this wavelength, the absorption depth τ in copper is 12.60 nm [10]. The laser intensity assumes a Gaussian temporal distribution in the form of

$$I=I_0e^{-(t-t_0)^2/t_1^2} \tag{4}$$

where t_0 and t_1 are taken as 10 ps and 3 ps, respectively, indicating that the laser pulse has an FWHM (full width at half maximum) of 5 ps centered at 10 ps. In this paper, the laser intensity used in Eqs. (3) and (4) is the one absorbed by the material rather than the incident laser intensity before reflection. Therefore, no reflectivity is used in Eq. (3).

In the second step of laser heating, the energy of free electrons is transferred to the lattice through electron-lattice coupling [1,6]

$$C_l\frac{\partial T_l}{\partial t}=k_l\frac{\partial^2 T_l}{\partial z^2}+G(T_e-T_l) \tag{5}$$

where C_l and k_l are the volumetric specific heat and the thermal conductivity of the lattice, respectively.

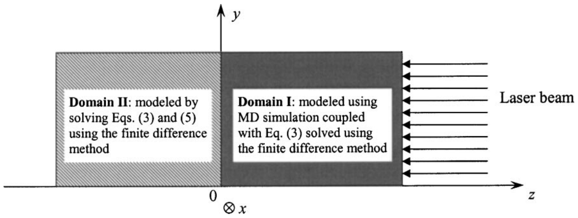

Fig. 1 Schematic of the computational domain

The schematic of the computational domain is shown in Fig. 1. An extra space is added above the target, which allows macromotion of atoms in the positive z-direction. The target is divided into two domains I and II as shown in Fig. 1. In Domain I the laser beam is absorbed and the target experiences intense thermal transport and phase change. In this domain, the movement of atoms is solved using MD simulation, which is described by Eq. (1). Since MD simulation can not capture the thermal transport by free electrons, Eq. (3) is solved using the finite difference method in this domain to predict the thermal transport by electrons. Equation (3) is integrated with MD simulation through the energy exchange between electrons and atoms (lattice). The lattice heating through the energy exchange with free electrons is achieved by exciting the kinetic energy of atoms in MD simulation, which is fulfilled by scaling the velocity of copper atoms with a factor χ

$$\chi=\left[1+\frac{\Delta t\cdot G(T_e-T_l)\cdot\Delta V}{\frac{1}{2}\sum_{i=1}^{N}m_i\cdot[(\nu_{i,1}-\overline{\nu_1})^2+(\nu_{i,2}-\overline{\nu_2})^2+(\nu_{i,3}-\overline{\nu_3})^2]}\right]^{1/2} \tag{6}$$

where $\nu_{i,j}$ and $\overline{\nu_j}$ ($j=1,2,3$) are velocities of atom i and the average velocity in the x, y, and z directions for atoms in a layer of volume ΔV normal to the laser beam. N is the number of atoms within the layer and Δt is the time step. The new velocity $\nu'_{i,j}$ of atom i is calculated as

$$\nu'_{i,j}=(\nu_{i,j}-\overline{\nu_j})\cdot\chi+\overline{\nu_j}\qquad j=1,2,3 \tag{7}$$

When density changes, such as void formation in the target, the electron-lattice coupling constant G is adjusted by multiplying a factor, which is the ratio of the local density to the full density of copper. In addition, the specific heat, density, and thermal conductivity of electrons are adjusted in the same manner. The density and specific heat of the lattice are computed by the MD simulation automatically, which directly tracks the movement of atoms. During the preparation of this paper, it came to our knowledge that laser-metal interaction was studied using the similar method as that described in this paper [11,12]. In these studies, the model developed by Häkkinen and Landman [2] was employed which added an extra term in Eq. (1) to account for the energy exchange between electrons and the lattice. Treatment of this lattice-electron coupling is different from the atomic velocity scaling described by Eq. (7) in this work, and does not the meet the requirement of momentum conservation, which may cause undesirable atomic movement.

In Domain II as shown in Fig. 1, heat transfer is calculated by solving Eqs. (3) and (5) using the finite difference method. This semi-infinite solid copper plays the role of conducting the heat away from Domain I, which experiences intense phase change. For atoms close to the back side of Domain I, two extra forces arise in the presence of the semi-infinite solid copper. One force originates from the static interaction between the MD domain and the semi-infinite solid sample. The static interaction represents the interaction between atoms in Domain I and those in Domain II when there is no stress in space. We place a layer of static atoms with a thickness of the cutoff distance in Domain II next to the interface between Domains I and II. The force exerted by atoms in

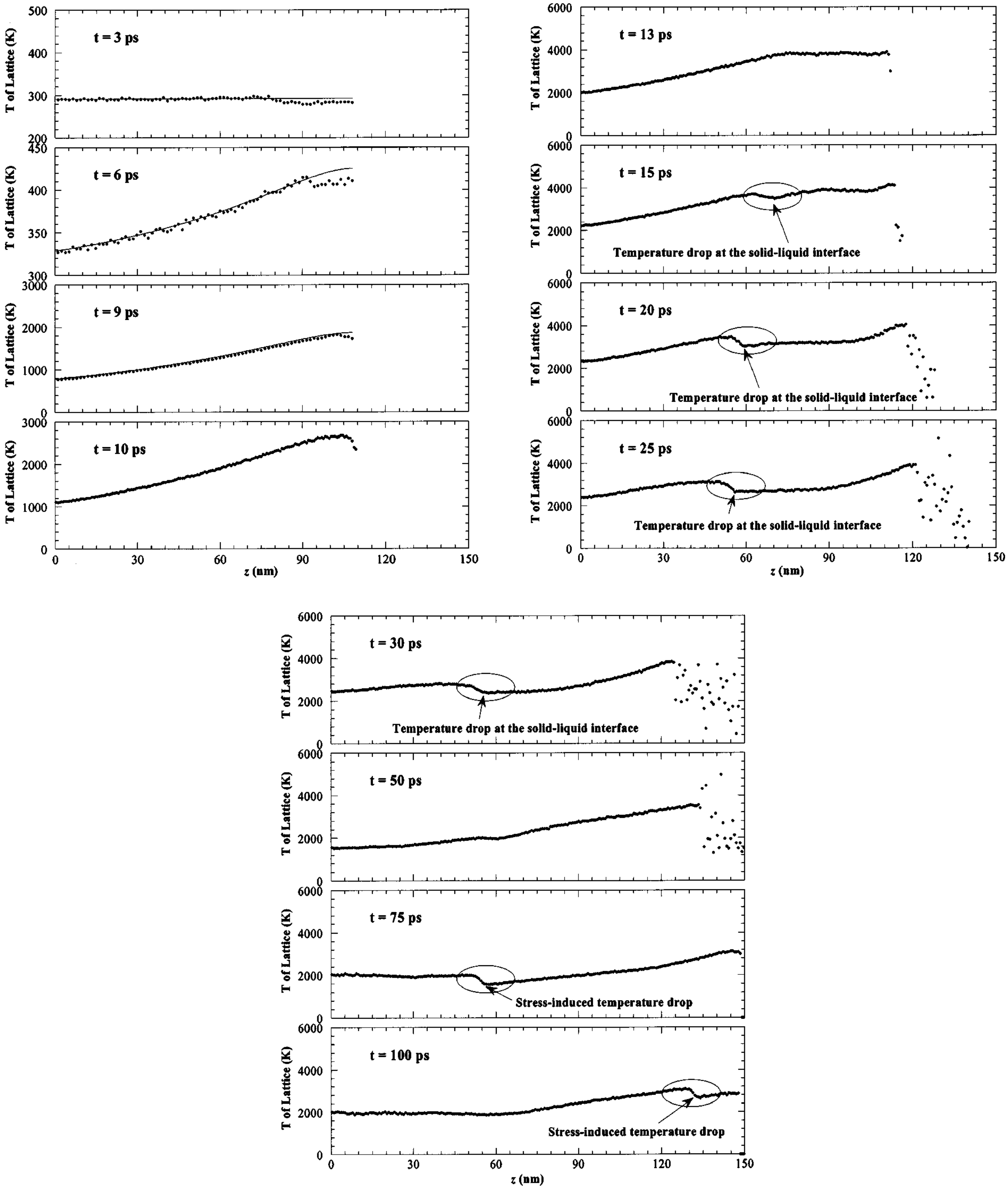

Fig. 2 The temperature distribution of lattice at different times. Solid line: numerical computation using the finite difference method; dots: MD simulation.

Domain II on those in Domain I represents the static interaction. The other force exerted on atoms in Domain I close to the interface between Domains I and II is induced by the stress wave propagation in the *z*-direction and is in the form of [13]

$$F_s = -\rho v c \cdot A/N \tag{8}$$

where ρ is the density of the target, v is the average velocity in the *z* direction for atoms within one small layer close to the back side, and *c* is the speed of the stress wave in the *z*-direction. *A* is the cross-sectional area of the target, and *N* is the number of atoms within the small layer close to the back side of Domain I. Periodic boundary conditions are implemented on boundaries in the *x* and *y* directions and free boundary conditions on boundaries in the *z*-direction.

When solving Eq. (3) in Domain I and Eqs. (3) and (5) in Domain II, constant properties are used, which are evaluated at 300 K. In the MD simulation part, introduction of Eq. (3) is used to consider the effect of heat transfer by electrons, which could not be accounted for by the classical MD simulation. It is true that the properties such as thermal conductivity and specific heat of electrons are temperature dependent. This paper presents our first step to study laser-metal interactions and we assume these prop-

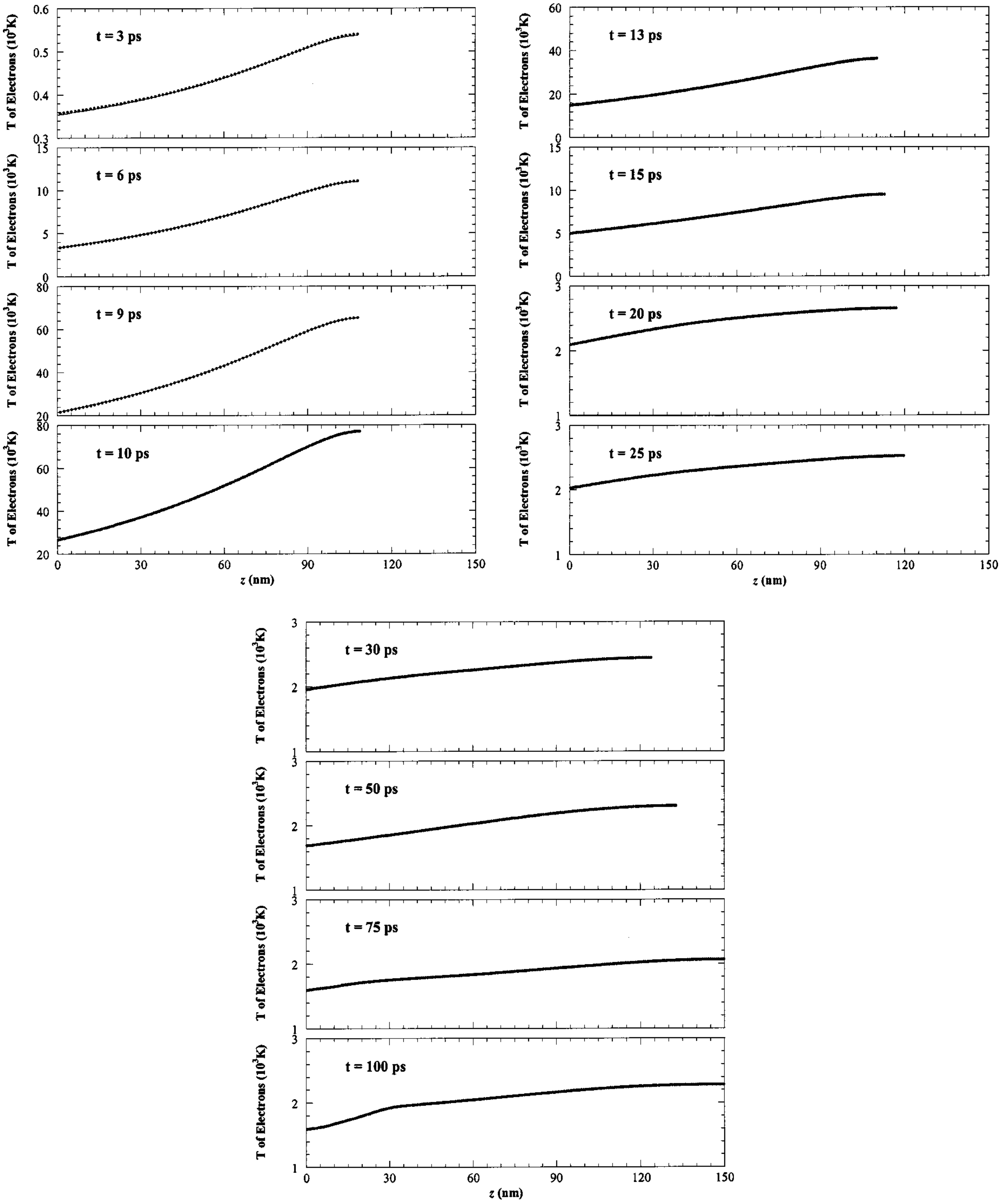

Fig. 3 The temperature distribution of electrons at different times. Solid line: numerical computation using the finite difference method; dots: MD simulation.

erties constant to simply the computation and provide a general picture about the physical processes underlying laser-metal interaction. These assumptions may affect the simulation results to a certain extent, but will not alter the general conclusions made in the paper, which is intended to provide qualitative interpretations of laser-metal interaction. In the laser-copper interaction studied in this work, intense phase change takes place in the material, which absorbs substantial thermal energy from electrons. This will reduce the uncertainty in heat conduction induced by the assumption of constant properties of electrons. Equations (3) and (5) are solved to obtain the temperature distribution in Domain II as specified in Fig. 1. Domain II is used to conduct the thermal energy from the MD domain (Domain I). The temperature distribution in Domain II is largely influenced by the thermal conductivity of electrons and the density and specific heat of the lattice. Therefore, the assumption of constant specific heat of electrons in Domain II has little effect on temperature distribution while at most times electrons and the lattice have close temperatures. In addition, the density and specific heat of the lattice and the thermal conductivity of electrons from 300 K to the melting point are pretty much constant.

Before laser heating starts, the sample is thermalized for 100 ps

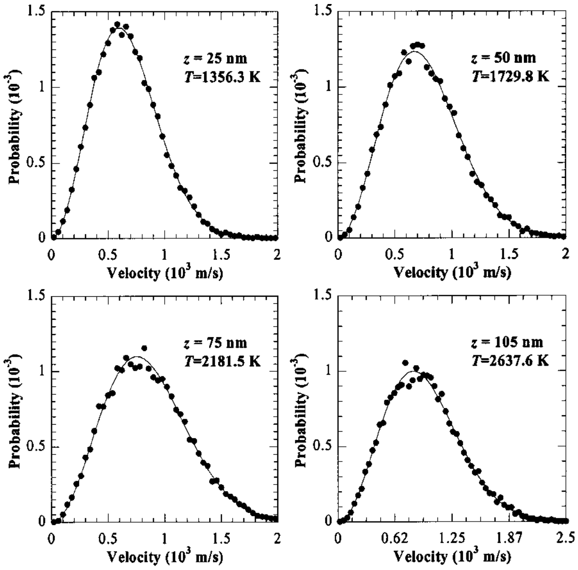

Fig. 4 Velocity distribution in comparison with the Maxwellian distribution at different locations during laser heating ($t = 10$ ps). The temperature shown in the figure is the local temperature used for calculating the Maxwellian distribution. Dots: MD simulation; solid line: Maxwellian distribution.

to reach thermal equilibrium. In this calculation, the MD domain is initially constructed based on the fcc lattice structure with the (100) surface facing the laser beam. Values of the parameters used in the simulation are listed in Table 1 [3,10,14–17]. The computation is conducted on a two-processor workstation using OpenMP (open multiple processing) as the algorithm for parallel computation. Before conducting simulation of laser-copper interaction, we calculate the specific heat and melting point of copper to obtain the idea about the accuracy of the Morse potential in terms of predicting the behavior of copper. The specific heat of copper is calculated by adding a certain amount of energy to a copper system and observing the final temperature increase. The specific heat is calculated to be 405 J/kg·K at 300 K, which is close to the experimental result of 385 J/kg·K [17]. The melting point of copper is obtained by increasing the temperature of a copper system until the regular lattice structure is completely destroyed. We find that the Morse potential predicts a melting point of 2090 K, higher than the experimental value of 1385 K [17].

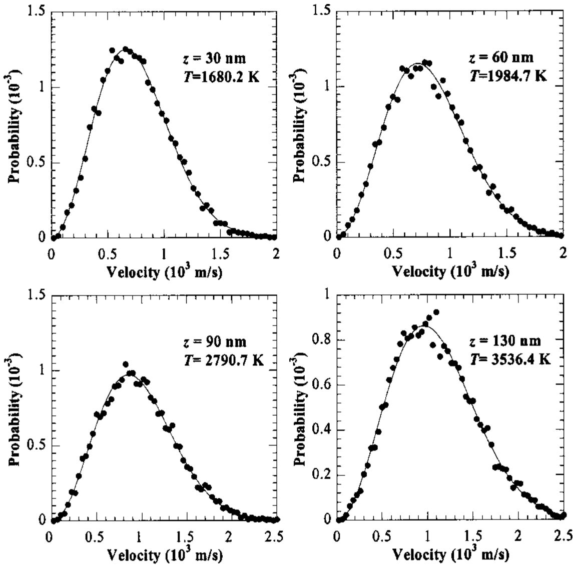

Fig. 5 Velocity distribution in comparison with the Maxwellian distribution at different locations after laser heating ($t = 50$ ps). The temperature shown in the figure is the local temperature used for calculating the Maxwellian distribution. Dots: MD simulation; solid line: Maxwellian distribution.

III Results and Discussion

In this work, the target for MD simulation is constructed to have 45, 45, and 300 fcc (face-centered cubic) unit cells in the x, y, and z-directions, respectively. A total of 2,430,000 atoms are tracked in the simulation. Measurements of the MD domain are 16.245 nm in the x and y directions, and 108.3 nm in the z-direction. The computational domain has the same size as the target in the x and y-directions. In the z-direction, the computational domain is taken as 2.608 μm to capture atoms escaping from the target surface during the time of computation. The laser pulse assumes a fluence (E) of 2000 J/m^2, which is estimated to be high enough to induce phase change and material ablation. At this laser fluence, the constant (I_0) in the temporal laser intensity expressed by Eq. (4) is $I_0 = E/(\sqrt{\pi}t_1) = 37.6126$ GW/cm^2.

III.1 Temperature Distribution in the Target. The temperature distribution in the lattice is displayed in Fig. 2. For the purpose of comparison, Eqs. (3) and (5) have been solved in Domain I using the finite difference method before phase change takes place. The results obtained using the finite difference method are shown at 3, 6, and 9 ps at which little or no phase change is observed. It is much pronounced that before phase change takes place, the MD simulation and the finite difference method are in good agreement in terms of predicting laser heating and thermal transport. Beyond 9 ps, phase change originates so only the MD simulation results are presented in Fig. 2. Before 13 ps, the temperature of the lattice experiences a continuous increase. However, it is important to note that when the lattice temperature reaches about 3850 K ($t = 13$ ps), no further temperature increase is observed. This phenomenon is clearly demonstrated by the temperature distribution at 13 ps for which a flat region of 3850 K is observed. The phase change from solid to liquid (detailed in III.2) absorbs a great deal of energy deposited by the laser beam, thereby suppressing further increase of the lattice temperature.

A close look at Fig. 2 reveals that starting from 15 ps (just after laser heating), a temperature drop appears in the spatial distribution. This temperature drop becomes abrupt at 20 and 25 ps, which is marked by circles in Fig. 2. As will be discussed below, this temperature drop originates from the phase change from solid to liquid. Further study finds that the location of this abrupt temperature change is the same as the location of the solid-liquid interface. The energy absorbed by the liquid during phase change explains the temperature drop observed in Fig. 2. At 13 ps in Fig. 2, a sudden temperature drop is not visible although a solid-liquid interface is observed in Fig. 6. This is because that at 13 ps, the material is still experiencing intense laser heating, which can provide the energy needed for melting. In addition, we find that before (including) 12 ps, no clear solid-liquid interface is observed although the front of the material is being melted. It is the movement of the solid-liquid interface (meaning melting is taking place) that induces the local temperature drop. At 13 ps, the solid-liquid interface starts to move, which takes time to induce the local temperature drop.

We study the melting point of the copper modeled using the Morse potential and find that this potential overpredicts the melting point and reports a value of 2090 K, higher than the melting point of copper [17]. At the solid-liquid interface, it is observed that the local temperature is greatly above 2000 K, exceeding the modeled melting point. Super heating has also been observed in the recent work by Schäfer et al. [11]. In addition to the temperature change resulting from phase change before 75 ps, another sudden temperature change has been observed after phase change

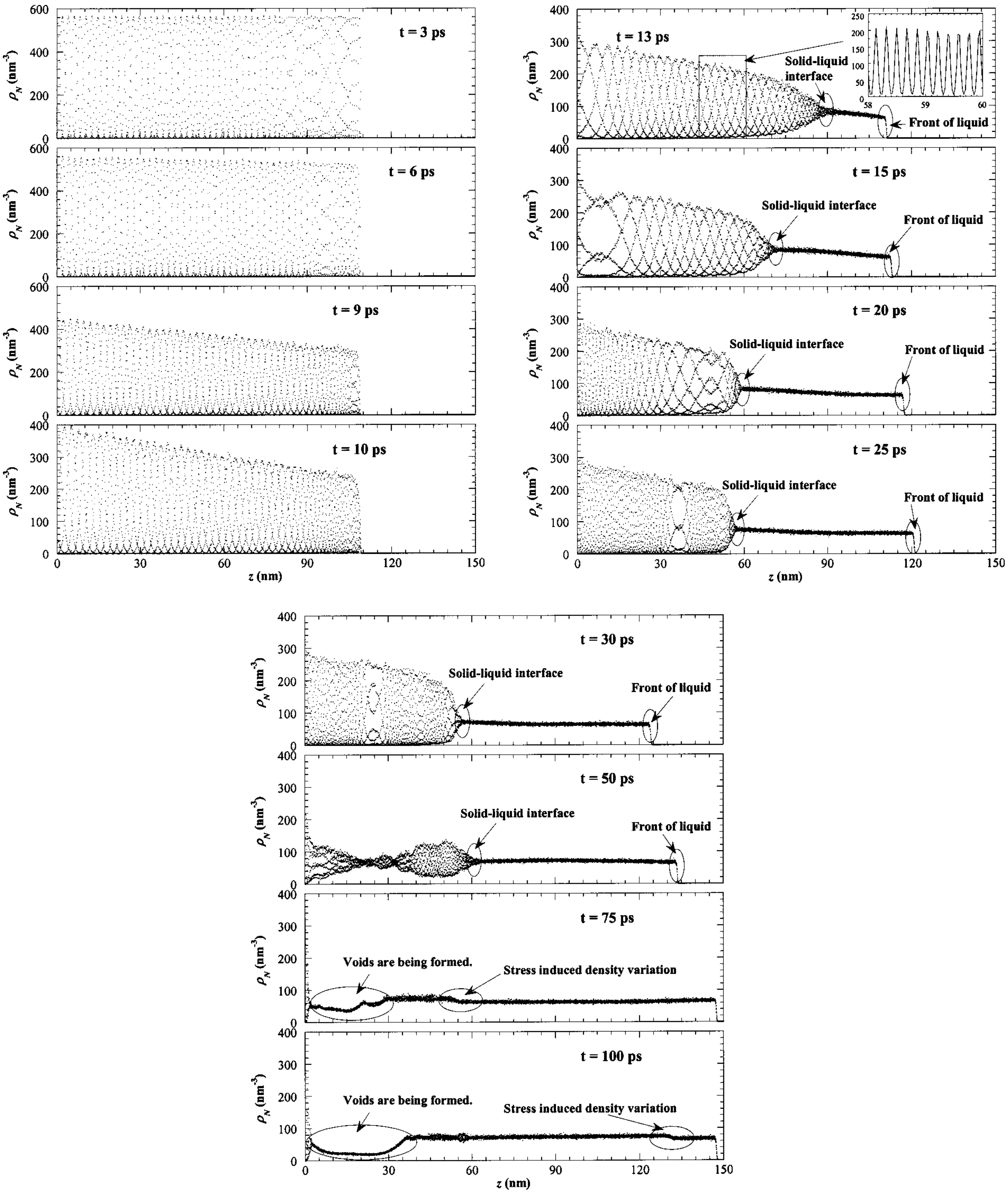

Fig. 6 Number density distribution in space at different times

finishes, which is marked by circles in Fig. 2 at 75 and 100 ps. This temperature change is a direct consequence of the sharp stress variation in space and will be discussed in III.3.

Presented in Fig. 3 is the temperature distribution of electrons. At 3, 6, and 9 ps, the MD simulation results are compared with those obtained with the finite difference method, and good agreements are observed. The temperature of electrons is characterized with a maximum level of about 78,000 K at 10 ps. At 15 ps (just after laser heating), the electron temperature quickly decreases to 10,000 K due to the intense energy exchange with the relatively cold lattice. From 15 ps to 20 ps, the temperature of electrons quickly decays to below the lattice temperature. Subsequently, electrons play the role of cooling the lattice and transferring the energy to the inside of the target.

When calculating the energy transfer from electrons to atoms in Domain I, the technique (Eqs. (6) and (7)) used to excite the kinetic energy of atoms meets the requirement of momentum conservation, but could disturb the local thermal equilibrium. The use of temperature to describe laser induced heating and thermal transport within the target can be justified by looking into the thermal equilibrium of the target during and after laser heating. Figure 4 shows the velocity distribution at different locations at 10

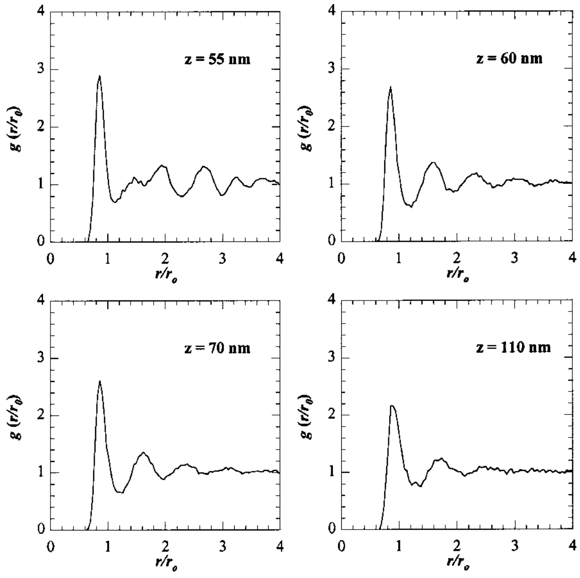

Fig. 7 In-plane radial distribution function at different locations for $t=20$ ps

ps (during laser heating). Also shown in Fig. 4 is the Maxwellian distribution in comparison with the MD results. It is evident that the velocity distribution of atoms follows the Maxwellian distribution closely, even at the very front of the target ($z=105$ nm). The equilibrium status of the target after laser heating is examined by comparing the velocity distribution of atoms with the Maxwellian distribution at different locations, including the front of the target ($z=130$ nm) at 50 ps. The comparison is presented in Fig. 5, which shows a good agreement between the atomic velocity distribution and the Maxwellian distribution, thereby confirming the existence of thermal equilibrium within the target and justifying the use of temperature.

III.2 Structural Change of the Target. In this section, the structural change within the target is investigated by looking into the number density distribution of atoms in space and the radial distribution function at different locations.

The number density is a measure of the number of atoms per unit volume. Its variation in space reflects the structural variation of the target [18]. Figure 6 presents the number density distribution at different times. In Fig. 6, no obvious solid-liquid interface is observed before 10 ps. At 13 ps, melting has happened, and a clear solid-liquid interface is evident, which is circled in the plot. The number density distribution in solid (to the left of the circle) has a regular pattern and is detailed in the inset. The periodically varying number density is attributed to the regular structure of the lattice. To the right of the circle is liquid, and its number density is uniform, which is a result of the random distribution of liquid atoms in space. It is apparent in Fig. 6 that the solid-liquid interface is moving toward the solid, meaning more solid is being melted. At the same time, a visible movement of the liquid front toward the right is observed, which is circled in the plot. When solid melts, its density becomes less, and the volume of the material will expand, thereby inducing the toward-out movement of the liquid front. The number density distribution at 50 ps reveals that solid and liquid structures co-exist in the rear part of the target, meaning melting takes place in this region simultaneously and is not characterized by a clear movement of the solid-liquid interface. This phenomenon could be attributed to the small thickness of the target and the boundary condition applied to the interface between Domains I and II. For instance, the reflected stress wave from the interface can strongly disturb the material close to the interface, making them melt simultaneously. We have performed large-scale parallel MD simulations to study this boundary and thickness effect. The target used is about 1.234 μm (consisting of more than 27 million atoms), which is more than ten times the thickness of the target studied in this work. In this extended study, no finite difference domain is added below the MD domain and a free boundary condition is employed. The results show that melting is characterized with a rapid movement of the solid-liquid interface, and no simultaneous melting is observed.

At 75 ps, the target has been melted completely, and the visible low number density in space is attributed to the formation of voids within the liquid. More details will be discussed in III.4. Furthermore, an insignificant, yet visible number density variation is observed at 75 and 100 ps. This number density change originates from the sharp stress change in space and is explained in detail in III.3. Based on locations of the solid-liquid interface and the front of liquid at 13 and 20 ps, it is estimated that during this period, the solid-liquid interface moves at a speed of 4400 m/s, and the front of the liquid moves out at a speed of 860 m/s. The calculated speed of the solid-liquid interface (~4400 m/s) is close to the sound speed in the [100] direction in copper (4364 m/s) [10]. Similar high-speed movement of the melt front was observed in the MD simulation about picosecond laser-copper interaction [11]. In that work, Schäfer et al. [11] reported a melt front velocity of the order of $1\text{-}2\times10^3$ m/s in a copper irradiated with a laser pulse of 0.5 ps duration and 680 J/m^2 fluence (absorbed).

In addition to the number density distribution, the radial distribution function also reflects the structure of the target. In this work, the in-plane radial distribution function $g(r/r_0)$ [18] is studied, which is a ratio of the number of atoms at a distance r from a given atom to the number of atoms at the same distance in an ideal gas with the same density. Figure 7 presents the in-plane radial distribution function at 20 ps. It is revealed that to the left of the solid-liquid interface, the radial distribution function is characterized with a number of peaks ($z=55$ nm), which are attributed to the regular structure of the solid. At locations of 60 nm and 70 nm (to the right of the solid-liquid interface), the short range order structure is still preserved while the long-range order is disappearing. This is reflected by the diminishing peaks at the long distance ($r/r_0=3$ or greater), meaning the materials are losing the long-range order structure. At the front of the liquid ($z=110$ nm), a typical liquid structure is observed, which is characterized by the two short-range peaks in the radial distribution function.

III.3 Stress Evolution in the Target. During laser material interaction, a stress wave will be generated and propagate toward the inside of the material. In this work, the stress is calculated based on the velocity and position of atoms. In the work by Wang and Xu [19], the stress was calculated by directly evaluating the atomic interaction force across a cross section of interest. Although the trend and amplitude of the stress were captured, substantial noise was observed in the calculation results. In this work, the stress is averaged over a small domain to suppress the statistical uncertainty following the equation

$$\sigma_{mn}=-\frac{1}{\Delta V}\left(\sum_{j\neq i}^{N} r_{ij,m}F_{ij,n}+\delta_{mn}\cdot Nk_BT\right) \tag{9}$$

where $r_{ij,m}$ and $F_{ij,n}$ are the distance and force between atoms i and j in the m and n directions, respectively. N is the number of atoms within a small domain of a volume ΔV. δ_{mn} is the delta function, which is 1 for $m=n$ and 0 for $m\neq n$. In the beginning of laser heating, the normal stress is the same in the x, y and z directions, and the shear stress is negligible. However, when voids are formed in the target, the shear stress becomes appreciable and the normal stress is not the same in the x, y and z directions. This issue will be addressed elsewhere. In this work, only the normal stress in the z direction (the laser irradiation direction) is discussed in detail. Figure 8 shows the stress wave generation and propagation in the copper target. At 3 ps, laser

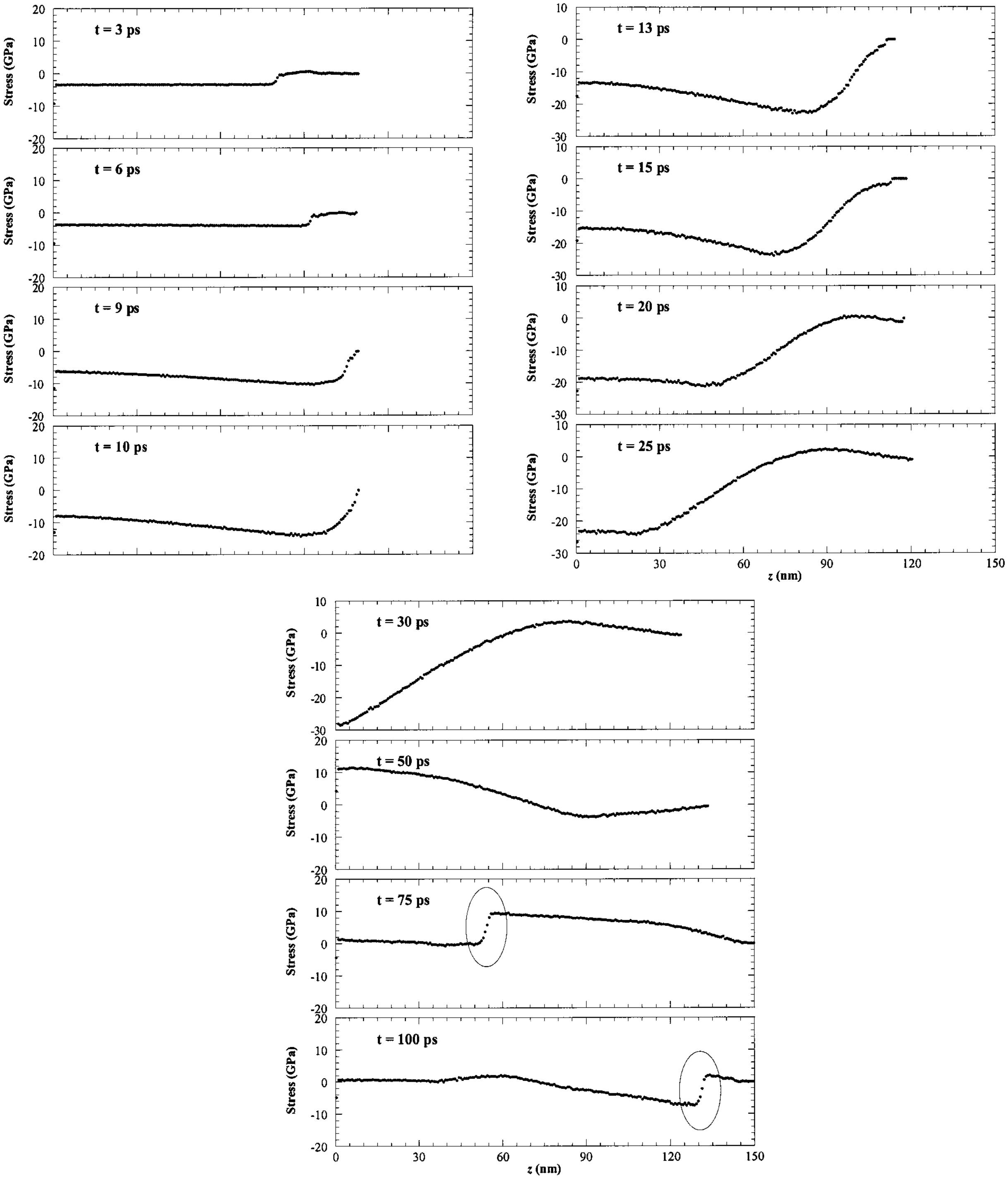

Fig. 8 Stress distribution in space at different times

heating is weak, and the visible non-zero stress originates from the initial construction of the target. At 9 ps, it is seen that a compressive stress has been generated in the near surface region. From 9 ps to 20 ps, the stress wave experiences an emerging process. At 25 ps, it is apparent that the stress wave consists of a strong compressive stress (~25 GPa) and a weak tensile stress (~3 GPa). This stress wave generation has the same characteristic as the one revealed in ps laser argon interaction [19]. In the MD simulation, we carefully monitor the development and propagation of the initial non-zero stress and find that this stress is induced by the design of the initial sample. This stress propagates in space with the same amplitude and does not cause structural damage. In addition, we conduct large-scale parallel MD simulation and observe the similar behavior of the nonzero initial stress. In the large-scale MD simulation, we used a much larger target (1.234 μm of thickness). A similar nonzero initial stress was observed with the same amplitude as the one observed in this paper. Our large-scale MD simulation with free boundary conditions indicates similar stress as the one observed in this work before reflection at the back side of the MD domain. This ensures that the large compressive stress observed in this work arises from the laser-material interaction and is not an amplification of the initial stress by the boundary conditions.

At 30 ps in Fig. 8, the compressive stress has reached the back

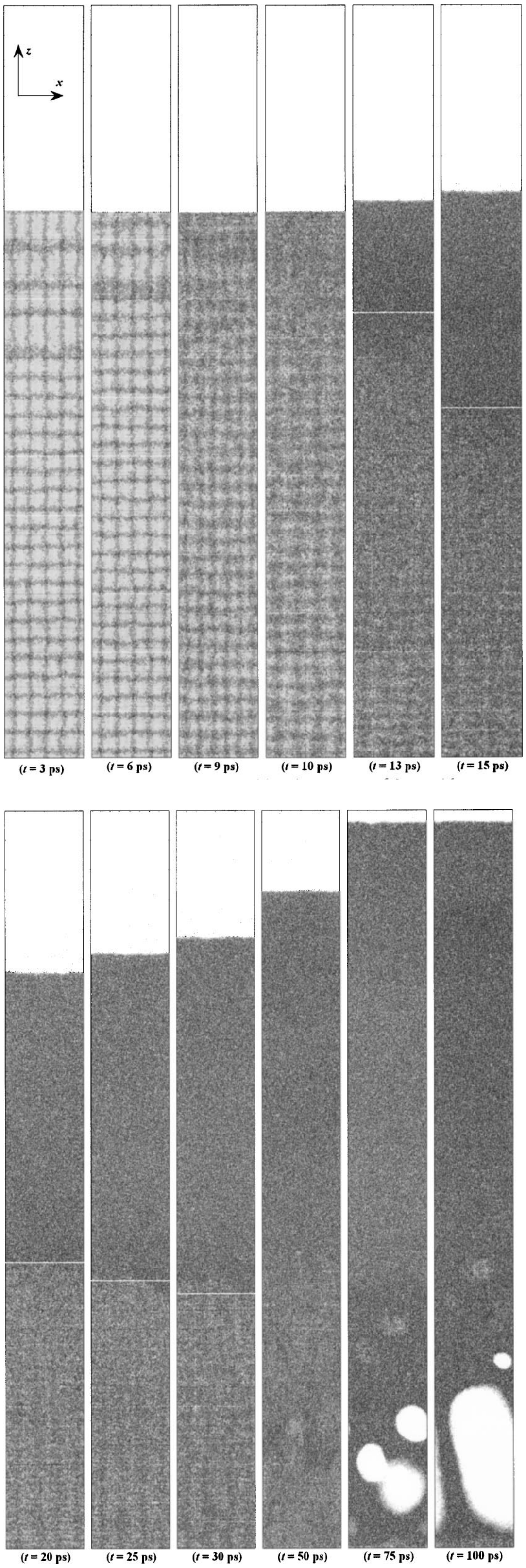

(t = 3 ps) (t = 6 ps) (t = 9 ps) (t = 10 ps) (t = 13 ps) (t = 15 ps)

(t = 20 ps) (t = 25 ps) (t = 30 ps) (t = 50 ps) (t = 75 ps) (t = 100 ps)

Fig. 9 Snapshot of atomic positions in the space of $0<x<16$ nm, $7.37<y<8.87$ nm, and $0<z<150$ nm. The horizontal white lines mark the approximate position of the solid-liquid interface.

side of the MD domain and is being reflected back. The boundary condition introduced by Eq. (8), which is intended to eliminate the reflection of the stress wave, could not eliminate the stress wave reflection completely. The speed c used in Eq. (8) is taken as 4364 m/s by assuming the target is a solid copper at room temperature [10]. On the other hand, in Figs. 2, 6, and 8 it is evident that when the stress wave reaches the back side ($t=30$ ps), the target is at a much elevated temperature (~2400 K) and has been melted partially. Based on the location of the peak compressive stress at 13 and 25 ps, it is estimated that the stress wave is traveling at a speed of about 5000 m/s, a little higher than the one used in Eq. (8). In addition, because of the much elevated temperature in Domain I, the spacing between atoms in this domain changes much, which is much different from the constant atomic spacing used in Domain II. Therefore, this structure mismatch will have a contribution to the wave reflection at the interface. Nevertheless, the boundary condition expressed by Eq. (8) does reduce the stress wave reflection, which is dictated by the smaller magnitude of the reflected stress (~10 GPa) compared with the larger magnitude of the incident stress (~28 GPa).

In Fig. 8, it is evident that after reflection, the compressive stress becomes a tensile stress. It has been observed in previous research that with a free boundary condition at the back side of the target, the stress wave is completely reflected [19]. After reflection, the speed of the stress wave reduces to 3080 m/s, much smaller than the speed of the incident stress wave. This could be explained by the fact that after 75 ps, the target has been melted completely, and the liquid sustains a lower wave speed than the solid does. Propagation of the reflected tensile stress is characterized with a substantial dissipation. At 75 ps, the tensile stress has a magnitude of 10 GPa located at 55 nm, while after only 25 ps, its magnitude decays to 2 GPa after traveling only about 77 nm. This reveals the fact that liquid has a limited capability of sustaining tensile stress waves. In addition, our careful study of the wave propagation from 75 ps to 100 ps reveals that there is a strong interaction between the reflected stress wave and the incident stress wave. This is because the stress generated by laser heating has a great span in space, making the reflected wave interact with the incident wave, complicating the stress distribution in space. At 75 and 100 ps, one abrupt change of the stress in space is observed, which is marked with circles in Fig. 8. This abrupt stress change could be attributed to some stress reflection at the interface between Domains I and II and the interaction between the reflected stress and the incident stress. This abrupt stress change means a rapid temporal stress variation at the local position, thereby inducing the sudden temperature change observed in Fig. 2. This temperature change is related to the local stress as [19]

$$\partial T_l/\partial t \sim -B/(B+4/3\cdot G)\cdot \beta_T T_0/(\rho c_p)\cdot \partial \sigma/\partial t \qquad (10)$$

Equation (10) has been discussed by Wang and Xu in detail elsewhere [19]. In this stress-temperature relation, B, G, β_T, ρ, c_p are the bulk and shear moduli, the thermal expansion coefficient, density and specific heat of the material, respectively. In addition to the induced temperature variation, the abrupt stress change marked in Fig. 8 at 75 and 100 ps also induces a visible variation of the number density of atoms, which is marked in Fig. 6. The tensile stress intends to pull the material apart, thereby inducing a visible number density drop.

III.4 Snapshots of Atomic Positions. Figure 9 presents the snapshots of atomic positions at different times with each dot representing one atom. For the purpose of illustration, only the domain of $0<x<16$ nm, $7.37<y<8.87$ nm, and $0<z<150$ nm is displayed in Fig. 9. It is apparent that at 3 and 6 ps, a regular structure is observed. Although the regular lattice structure is still preserved at 9 and 10 ps, atoms spread more in space, especially in the near surface region. This is because the temperature of the target is increasing due to laser heating, thereby resulting in a more intense random movement of atoms and spreading them more in space. This reduction of the structural regularity explains the decay of the peak number density of atoms, especially in the near surface region as observed at 9 and 10 ps in Fig. 6. At 13 ps, it is apparent that in the near surface region, positions of atoms become completely random, meaning the target has lost the regularity of the structure, and solid no longer exists in this region.

At 20, 25, and 30 ps, a clear solid-liquid interface is much pronounced, which is marked with a white horizontal line. In the liquid region, atoms become random in space, and the picture looks dark. On the other hand, the picture looks light in the solid region due to the regular position of atoms in space. An interesting phenomenon is observed at 75 and 100 ps, which is characterized with voids formed inside the liquid. The tensile stress has a great contribution to the formation of voids because the tensile stress intends to pull the atoms apart in the material. At 75 and 100 ps, the material is liquid which has limited capability of sustaining tensile stress and the atoms inside are easy to be pulled apart. The existence of this tensile stress is a direct consequence of the reflection of the compressive stress at the back side of the MD domain. This suggests that in laser materials interaction, especially for thin films deposited on substrates or for free-standing thin films, the reflection of the compressive stress at the back side of the film makes the compressive stress become tensile; this tensile stress could result in a structural damage in the region close to the back side.

IV Conclusion

In this work, MD simulation was carried out to investigate the thermal and thermomechanical phenomena in ps laser copper interaction. Superheating was observed, and the early period of phase change from solid to liquid was characterized with a solid-liquid interface movement at a speed of 4400 m/s. However, the latter phase change from solid to liquid happened in the target simultaneously with no visible movement of solid-liquid interface. The results showed that the laser induced stress wave consisted of a strong compressive stress and a weak tensile stress. The strong tensile stress emerging after stress wave reflection at the back side of the MD domain exceeded the limitation that can be sustained by the target and intended to pull the material apart. As a direct consequence, voids were formed in the interior of the liquid near the back side of the MD domain, indicating that the strong tensile stress in laser materials interaction played an important role in inducing structural defect in the target. Propagation of this strong tensile stress was characterized with a remarkable decay, which could be attributed to the limited capability of liquid to sustain tensile stress waves and the interaction between the reflected and incident stress waves.

Acknowledgment

Financial support for this work from the College of Engineering and Technology and the Department of Mechanical Engineering at the University of Nebraska–Lincoln (UNL) is greatly acknowledged. This work is also partially supported by the Research Council of UNL through the Faculty Seed Grant. The author thanks Dr. Xianfan Xu of Purdue University and Dr. David A. Willis of the Southern Methodist University for their helpful discussions.

Nomenclature

A = cross-sectional area
B = bulk modulus
C_e = volumetric specific heat of free electrons
C_l = volumetric specific heat of lattice
c = stress wave speed
D = dissociation energy
F = interaction force between atoms
F_s = the force induced by stress wave propagation
G = electron-lattice coupling factor; shear modulus
g = radial distribution function
I = laser beam intensity
I_0 = constant in the laser intensity temporal distribution
k_e = thermal conductivity of free electrons
k_l = thermal conductivity of lattice
m = atomic mass
N = number of atoms
r = atomic position
r_c = cutoff distance
r_0 = equilibrium distance
T_e = temperature of free electrons
T_l = temperature of lattice
t = time
t_0 = time constant in the laser intensity temporal distribution
t_1 = time constant in the laser intensity temporal distribution
ν = velocity
x = coordinate in the x direction
y = coordinate in the y direction
z = coordinate in the z direction

Greek Symbols

α = constant in the Morse potential
β_T = thermal expansion coefficient
ϕ = Morse potential function
ρ = density
σ = stress
τ = laser beam absorption depth

Subscripts

i = index of atoms

References

[1] Anisimov, S. I., Kapeliovich, B. L., and Perelman, T. L., 1974, "Electron Emission from Metal Surfaces Exposed to Ultra-short Laser Pulses," Sov. Phys. JETP, **39**, pp. 375–377.

[2] Häkkinen, H., and Landman, U., 1993, "Superheating, Melting, and Annealing of Copper Surfaces," Phys. Rev. Lett., **71**, pp. 1023–1026.

[3] Girifalco, L. A., and Weizer, V. G., 1959, "Application of the Morse Potential Function to Cubic Metals," Phys. Rev., **114**, pp. 687–690.

[4] Horiuchi, K., Ishiyama, M., Hasebe, T., Yukimura, K., and Imaida, Y., 1998, "A Fundamental Study of Excimer Laser Ablation Using Experimental and MD Simulation Method," Mater. Chem. Phys., **54**, pp. 201–204.

[5] Ohmura, E., Fukumoto, I., and Miyamoto, I., 1999, "Modified Molecular Dynamics Simulation on Ultrafast Laser Ablation of Metal," presented at the International Congress on Applications of Lasers and Electro-Optics, Laser Institute of America, Orlando, pp. 219–228.

[6] Qiu, T. Q., and Tien, C. L., 1993, "Heat Transfer Mechanisms During Short-Pulse Laser Heating of Metals," ASME J. Heat Transfer, **115**, pp. 835–841.

[7] Tang, D. W., and Araki, N., 1996, "The Wave Characteristics of Thermal Conduction in Metallic Films Irradiated by Ultra-short Laser Pulses," J. Phys. D, **29**, pp. 2527–2533.

[8] Wang, X., and Xu, X., 2002, "Thermoelastic Wave in Metal Induced by Ultrafast Laser Pulses," J. Therm. Stresses, **25**, pp. 457–473.

[9] Allen, M. P., and Tildesley, D. J., 1987, *Computer Simulation of Liquids*, Clarendon Press, Oxford.

[10] Lide, D. R., 1994, *CRC Handbook of Chemistry and Physics: A Ready-Reference Book of Chemical and Physical Data*, Section 12, CRC Press, Boca Raton, FL.

[11] Schäfer, C., Urbassek, H. M., and Zhigilei, L. V., 2002, "Metal Ablation by Picosecond Laser Pulses: A Hybrid Simulation," Phys. Rev. B, **66**, pp. 1–8.

[12] Ivanov, D. S., and Zhigilei, L. V., 2003, "Combined Atomistic-Continuum Modeling of Short-pulse Laser Melting and Disintegration of Metal Films," Phys. Rev. B, **68**, pp. 1–22.

[13] Zhigilei, L. V., and Garrison, B. J., 1999, "Pressure Waves in Microscopic Simulations of Laser Ablation," Mater. Res. Soc. Symp. Proc., **538**, pp. 491–496.

[14] Kittel, C., 1976, *Introduction to Solid State Physics*, 5th ed., John Wiley & Sons, New York.

[15] Lide, D. R., and Kehiaian, H. V., 1994, *CRC Handbook of Thermophysical and Thermochemical Data*, CRC Press, Boca Raton, FL.

[16] Tzou, D. Y., 1996, *Macro- to Microscale Heat Transfer-The Lagging Behavior*, Taylor and Francis, Washington.

[17] Incropera, F. P., and Dewitt, D. P., 2002, *Fundamentals of Heat and Mass Transfer*, 5th ed., John Wiley & Sons, New York.

[18] Wang, X., and Xu, X., 2002, "Molecular Dynamics Simulation of Heat Transfer and Phase Change During Laser Material Interaction," ASME J. Heat Transfer, **124**, pp. 265–274.

[19] Wang, X., and Xu, X., 2003, "Molecular Dynamics Simulation of Thermal and Thermomechanical Phenomena in Picosecond Laser Material Interaction," Int. J. Heat Mass Transfer, **46**, pp. 45–43.